

1 **Distinct Impacts of El Niño-Southern Oscillation and Indian Ocean Dipole**
2 **on China's Gross Primary Production**

3 Ran Yan^{1,2}, Jun Wang^{1,2*}, Weimin Ju^{1,2*}, Xiuli Xing³, Miao Yu⁴, Meirong Wang⁴, Jingye

4 Tan^{1,2}, Xunmei Wang^{1,2}, Hengmao Wang^{1,2}, Fei Jiang^{1,2}

5 ¹Frontiers Science Center for Critical Earth Material Cycling, International Institute for Earth System Science,
6 Nanjing University, Nanjing, Jiangsu 210023, China

7 ²Jiangsu Provincial Key Laboratory of Geographic Information Science and Technology, Key Laboratory for Land
8 Satellite Remote Sensing Applications of Ministry of Natural Resources, School of Geography and Ocean Science,
9 Nanjing University, Nanjing, Jiangsu 210023, China

10 ³Department of Environmental Science and Engineering, Fudan University, No. 2005, Songhu Road, Yangpu
11 District, Shanghai 200438, China

12 ⁴Joint Center for Data Assimilation Research and Applications/Key Laboratory of Meteorological Disaster,
13 Ministry of Education/Joint International Research Laboratory of Climate and Environment Change (ILCEC)/
14 Collaborative Innovation Center ON Forecast and Evaluation of Meteorological Disasters, Nanjing University of
15 Information Science and Technology, Nanjing 210044, China

16 Corresponding author: Jun Wang (wangjun@nju.edu.cn); Weimin Ju (juweimin@nju.edu.cn)

17

18 **Abstract**

19 Gross primary production (GPP), a crucial component in the terrestrial carbon cycle, is strongly
20 influenced by large-scale circulation patterns. This study explores the influence of El Niño-
21 Southern Oscillation (ENSO) and Indian Ocean Dipole (IOD) on China's GPP, utilizing long-
22 term GPP data generated by the Boreal Ecosystem Productivity Simulator (BEPS). Partial
23 correlation coefficients between GPP and ENSO reveal substantial negative associations in
24 most parts of western and northern China during the September-October-November (SON)
25 period of ENSO development. These correlations shift to strongly positive over southern China
26 in December-January-February (DJF), then weaken in March-April-May (MAM) in the
27 following year, eventually turning generally negative over southwestern and northeastern China
28 in June-July-August (JJA). In contrast, the relationship between GPP and IOD basically exhibits
29 opposite seasonal patterns. Composite analysis further confirms these seasonal GPP anomalous
30 patterns. Mechanistically, these variations are predominantly controlled by soil moisture during
31 ENSO events (except MAM) and by temperature during IOD events (except SON).
32 Quantitatively, China's annual GPP demonstrates modest positive anomalies in La Niña and
33 negative IOD years, in contrast to minor negative anomalies in El Niño and positive IOD years.
34 This outcome is due to counterbalancing effects, with significantly larger GPP anomalies
35 occurring in DJF and JJA. Additionally, the relative changes in total GPP anomalies at the
36 provincial scale display an east-west pattern in annual variation, while the influence of IOD
37 events on GPP presents an opposing north-south pattern. We believe that this study can
38 significantly enhance our understanding of specific processes by which large-scale circulation
39 influences climate conditions and, in turn, affects China's GPP.

40

41 **Key words:** Gross primary production, China, El Niño-Southern Oscillation, Indian Ocean
42 Dipole, BEPS

43

44 **1.Introduction**

45 Vegetation photosynthesis, a pivotal physiological process affecting the terrestrial carbon cycle,
46 predominantly governs variations in the net biome productivity (NBP), surpassing the impact
47 of total ecosystem respiration (Piao et al., 2020; Wang et al., 2022; Wang et al., 2018). Gross
48 primary production (GPP) represents the total amount of carbon dioxide assimilated by plants
49 per unit time through the photosynthetic processes, acting as a crucial carbon flux in mitigating
50 anthropogenic CO₂ emissions (Gough, 2012; Houghton, 2007). However, despite evident long-
51 term increasing trends in GPP, primarily attributed to CO₂ fertilization (Ryu et al., 2019;
52 Schimel et al., 2015; Yang et al., 2022), it also shows regional and global interannual variations.
53 These variations are largely linked to climate fluctuations driven by ocean-atmosphere
54 interactions and the teleconnections (Wang et al., 2021b; Ying et al., 2022). To date, the impact
55 of such teleconnections on China's GPP remains insufficiently documented.

56
57 The El Niño-Southern Oscillation (ENSO) exerts a significant influence on the global terrestrial
58 carbon cycle, which is the dominant mode of inter-annual climate variability (Bauch, 2020;
59 Kim et al., 2017; Wang et al., 2016; Wang et al., 2018; Zeng et al., 2005). Within this context,
60 GPP typically assumes a leading role in shaping the response of terrestrial carbon sinks to
61 ENSO events (Ahlstrom et al., 2015; Wang et al., 2018; Zhang et al., 2018). Global patterns
62 reveal a negative GPP anomaly of approximately $-1.08 \text{ Pg C yr}^{-1}$ during El Niño years,
63 contrasting a positive GPP anomaly of about $1.63 \text{ Pg C yr}^{-1}$ in La Niña years (Zhang et al.,
64 2019). However, the impact of ENSO on GPP exhibits significant regional differences. At
65 present, while existing researches have predominantly focused on the response of tropical GPP
66 to ENSO, studies specific to China are relatively limited. Liu et al. (2014) highlighted the effects
67 of ENSO on crop growth in the North China, and Li et al. (2021) demonstrated that the response
68 of GPP to El Niño varies with the phase of the Pacific Decadal Oscillation (PDO) in the eastern
69 China.

70
71 ENSO is not the sole global climatic oscillation, influencing the terrestrial carbon cycle.

72 Another significant player is the Indian Ocean Dipole (IOD), a tropical coupled ocean-
73 atmosphere mode (Saji et al., 1999), which also affects the terrestrial carbon cycling by
74 modulating the climate circulations (Wang et al., 2022; Wang et al., 2020; Wang et al., 2021b;
75 Yan et al., 2023). Research indicates that IOD events can influence precipitation in China, with
76 effects lasting from the year of the event through the subsequent summer (Zhang et al., 2022a).
77 Zhang et al. (2022b) also proved that extreme positive IOD (pIOD) events in 2019 affected the
78 precipitation in summer 2020 in Eastern China, and proposed that the summer precipitation in
79 the following year was mainly affected by IOD in northern China, while by ENSO in the
80 Yangtze River Basin. Additionally, a prior study explored the influence of the extreme
81 pIOD event in 2019 on GPP anomalies across the Indian Ocean rim countries. It suggested a
82 conspicuous negative GPP anomaly occurred in eastern China during the September-October-
83 November (SON) (Wang et al., 2021b).

84

85 The primary objective of this study was to comprehensively assess the impact of ENSO and
86 IOD events on GPP in China. To this end, we initially employed partial correlation analysis to
87 elucidate the relationship between GPP and climate anomalies, specifically soil moisture and
88 temperature, induced by ENSO and IOD events across various seasons. The analysis utilized
89 historical long-term GPP data spanning from 1981 to 2021, simulated by the Boreal Ecosystem
90 Productivity Simulator (BEPS) model. The aim was to get a preliminary understanding of the
91 influence exerted by ENSO and IOD. Furthermore, composite analysis was adopted to illustrate
92 the actual responses during distinct events, including individual ENSO and IOD occurrences.
93 The ensuing discussion will delve into the analysis results on national, regional, and provincial
94 scales.

95

96 **2.Datasets and methods**

97 **2.1 Datasets used**

98 The sea surface temperature (SST) dataset was derived from the Monthly NOAA's Extended
99 Reconstructed Sea Surface Temperature version 5 (ERSSTv5) (Muñoz, 2019). It is generated
100 on a $2^\circ \times 2^\circ$ grid, using statistical methods to enhance spatial completeness. Commencing from
101 January 1854 to the present, the monthly SST data includes anomalies computed with respect
102 to a 1971-2000 monthly climatology.

103

104 Meteorological data were adopted from ECMWF Reanalysis v5 (ERA5)-Land monthly
105 averaged data with $0.1^\circ \times 0.1^\circ$ grids, including 2m surface air temperature (TAS), and
106 volumetric soil moisture (SM) during the period from 1981 to 2021. ERA5-Land was created
107 by replaying the land component of the ECMWF ERA5 climate reanalysis at a higher resolution
108 compared to ERA5. Reanalysis combines model data with global observations into a consistent
109 dataset based on the laws of physics. The original soil moisture data was divided into four layers
110 based on different surface depths. These layers were depth-weighted and then aggregated into
111 the average soil moisture to a depth of 289cm ($\text{m}^3 \text{m}^{-3}$).

112

113 GPP spanning from 1981 to 2021 was simulated by the BEPS model, featuring a horizontal
114 resolution of $0.0727^\circ \times 0.0727^\circ$. The BEPS model, originally developed for Canadian boreal
115 ecosystems, has been re-constructed for GPP simulations on the global scale (Chen et al., 1999;
116 Chen et al., 2012). BEPS is a process-based model driven by satellite-observed leaf area index
117 (LAI) and foliage clumping index (Ω), meteorological data, land cover types, soil texture, and
118 CO_2 concentration to simulate the daily carbon flux of terrestrial ecosystems (Chen et al., 2019;
119 Liu et al., 1997). The input data used to drive GPP in this study include ERA5 meteorological
120 data (Hersbach et al., 2023), GLOBMAP LAI product (Liu et al., 2012), Land Cover
121 Classification System (LCCS) generated by the Food and Agriculture Organization (FAO) of
122 the United Nations (Friedl and Sulla-Menashe, 2019), Harmonized World Soil Database v1.2

123 from FAO (Fischer et al., 2008), and CO₂ concentration based on the Global Monitoring
124 Laboratory from NASA (Lan et al.).

125 Notably, BEPS distinguishes itself from other models through the organic combination of
126 remote sensing data and mechanistic modelling. It produces simulation datasets for GPP, Net
127 primary productivity (NPP), and evapotranspiration (ET). Key features of BEPS include the
128 incorporation of sunlit-shaded leaf stratification strategy (Norman, 1982). The model calculates
129 canopy-level photosynthesis by summing the GPP of sunlit and shaded leaves (Chen et al.,
130 1999).

$$131 \quad GPP = A_{sun}LAI_{sun} + A_{shade}LAI_{shade} \quad (1)$$

$$132 \quad LAI_{sun} = 2 \cos \theta \left[1 - \exp \left(- \frac{0.5\Omega LAI}{\cos \theta} \right) \right] \quad (2)$$

$$133 \quad LAI_{shade} = 1 - LAI_{sun} \quad (3)$$

134 where A_{sun} and A_{shade} represent the amount of photosynthesis at per sunlit and shaded leaf,
135 respectively; LAI_{sun} and LAI_{shade} represent the canopy-level sunlit and shaded LAI,
136 respectively; Ω is the foliage clumping index indicating the influence of foliage clustering on
137 radiation transmission, and θ is the solar zenith angle.

138

139 The accuracy of carbon flux products simulated by BEPS has been validated in previous studies
140 (Chen et al., 2019; He et al., 2021). We also used the measured site data from ChinaFlux
141 (<http://chinaflux.org/>) and National Tibetan Plateau Third Pole Environment (Li et al., 2013)
142 (Table S1) to assess the performance of BEPS simulated GPP (Fig. S1). Our analysis reveals a
143 high consistency between simulated and observed GPP, with an average R² of 0.77 ($p < 0.05$)
144 and an average root mean square error (RMSE) of 1.70 gC m⁻² day⁻¹. In addition, the global
145 terrestrial GPP from FluxSat product Version 2.2 (Joiner et al., 2018) was also used to assess
146 the reliability of BEPS GPP. FluxSat GPP is obtained by using light-use efficiency (LUE)
147 framework based on Moderate-resolution Imaging Spectroradiometer (MODIS) satellite data,
148 eliminating the dependency on other meteorological input data. The comparison between BEPS
149 GPP and FluxSat GPP data revealed a robust agreement, with a correlation coefficient (r) of
150 0.63 ($p < 0.05$) and a RMSE of 1.1 Pg C yr⁻¹ (Fig. S2). These consistencies underscore the

151 reliability of the BEPS GPP data in capturing terrestrial carbon flux dynamics.

152 **2.2 Anomaly calculation**

153 To calculate anomalies, we first removed the long-term climatology to eliminate the seasonal
154 cycle. Subsequently, we subtracted the 7-year running average for each grid to eliminate the
155 decadal oscillation and long-term trends for all the variables. Further, refinement involved
156 smoothing the derived GPP and climate anomalies using a 3-month running average to remove
157 the intra-seasonal variability. For consistency, the BEPS simulated GPP data was resampled to
158 $0.1^\circ \times 0.1^\circ$. To align with this, non-vegetated areas in the climate data were masked according
159 to the resampled BEPS GPP, uniformity in spatial representation.

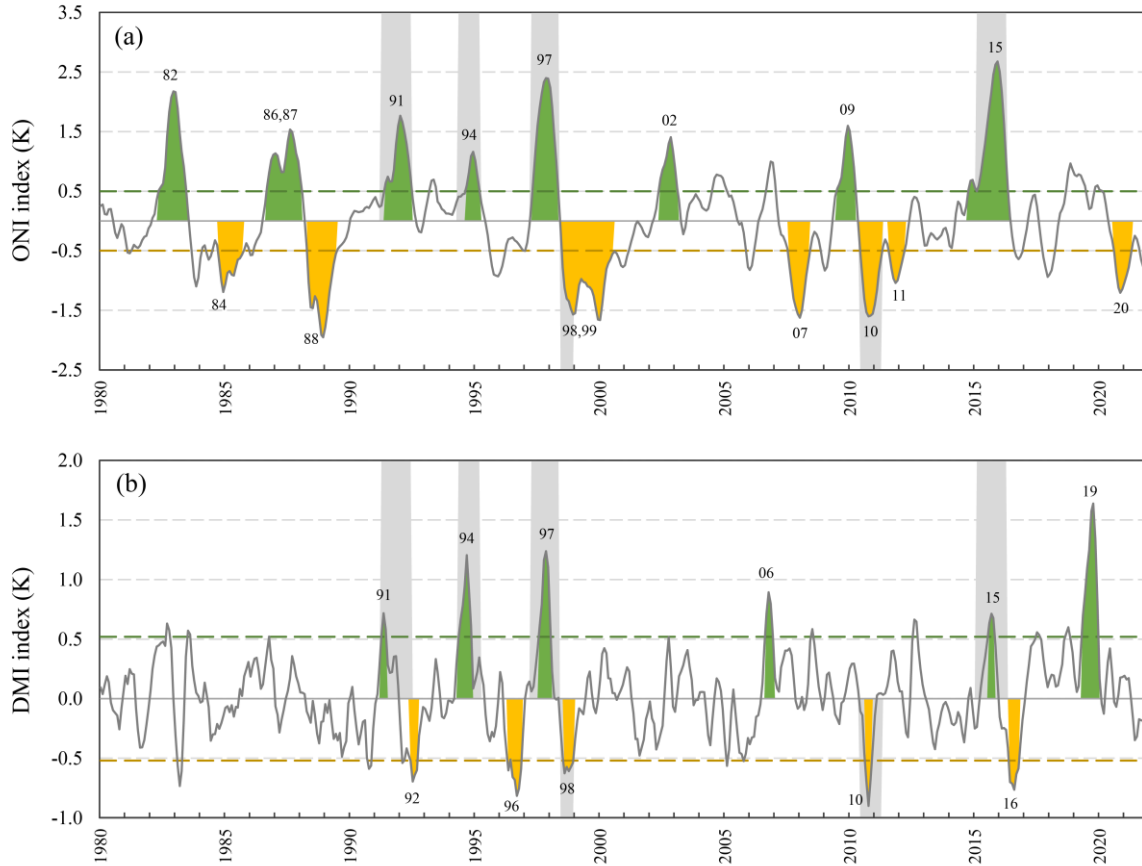
160 **2.3 Definition of climate events**

161 The Oceanic Niño Index (ONI) is used to define ENSO events (Fig. 1a), which represents the
162 3-month running mean SST anomaly in the Niño 3.4 region (5°N - 5°S , 120° - 170°W). The
163 positive phase of an ENSO event (El Niño) is characterized by the ONI exceeding $+0.5\text{K}$ for
164 five consecutive overlapping 3-month periods. Conversely, the negative phase of an ENSO
165 event (La Niña) occurs when the ONI is below -0.5K for five consecutive overlapping 3-month
166 periods. The severity of the event can be further categorized into weak ($0.5\sim 0.99$), moderate
167 ($1.00\sim 1.49$), strong ($1.50\sim 1.99$) and extremely strong (≥ 2.00) based on the absolute value of
168 the ONI. To qualify for a specific rating, an event should meet or exceed a threshold for at least
169 three consecutive overlapping three-month periods.

170

171 Moreover, the Dipole Mode Index (DMI) is employed to identify IOD events (Saji et al., 1999).
172 The DMI is calculated from SST differences between the Western Equatorial Indian Ocean
173 (10°S - 10°N , 50° - 70°E) and the South-eastern Equatorial Indian Ocean (10°S - 0°N , 90° - 110°E)
174 (Fig.1b). Given that the short duration of IOD events with a tendency to peak during the SON,
175 the standard deviation of SON DMI (0.52K from 1981 to 2021) is used as the criterion for
176 identifying IOD events. A positive phase IOD (pIOD) event is defined when the absolute value

177 of DMI is greater than or equal to one standard deviation (0.52 K) for three consecutive 3-
 178 month periods. Additionally, a strong pIOD event is identified if the DMI value exceeds two
 179 standard deviations (1.04 K).



180
 181 Fig.1 Time series of the Oceanic Niño Index (ONI) (a) and the Dipole Mode Index (DMI) (b) from 1980
 182 to 2022. The positive phase events (El Niño and positive Indian Ocean Dipole (pIOD)) are filled in
 183 green and the negative phase events (La Niña and negative IOD (nIOD)) are filled in yellow, and the
 184 events are also labeled with a two-digit year. The green and yellow dashed lines represent the positive
 185 and negative thresholds for El Niño-Southern Oscillation (ENSO) and IOD, respectively. The gray
 186 background indicates years with the simultaneous ENSO and IOD events.

187 2.4 Partial correlation analysis

188 To comprehensively assess the impacts of ENSO and IOD on GPP, while accounting for the
 189 influence of other events, partial correlation analysis (*pcor*) was employed, following the
 190 previous studies (Saji and Yamagata, 2003; Wang et al., 2021b). The definition of *pcor* for x

191 and y , controlling for z , is given by:

$$192 \quad pcor_{yx.z} = \frac{r_{yx} - r_{yz}r_{xz}}{\sqrt{1-r_{yz}^2}\sqrt{1-r_{xz}^2}} \quad (4)$$

193 where r_{yx} is the correlation of the dependent variable y and the explanatory variable x (e.g.,
194 DMI), and the same is for r_{yz} and r_{xz} . The two-tailed Student's t -test was used to calculate
195 the statistical significance of each pixel result:

$$196 \quad t = pcor_{yx.z} \sqrt{\frac{n-2-k}{1-pcor_{yx.z}^2}} \quad (5)$$

197 where n and k are the number of samples and conditioned variables, respectively.

198

199 **2.5 Composite analysis**

200 When enumerating the years of ENSO and IOD events, we retained all the years of IOD events
201 and ENSO events of above the moderate intensity. Individual events and compound events were
202 categorized and summarized in Table 1. In this study, a compound event refers to the
203 simultaneous occurrence of ENSO and IOD, primarily El Niño & pIOD and La Niña & negative
204 IOD (nIOD). IOD typically peaked in the September-October-November (SON, yr0), while
205 ENSO peaked in the December(yr0)-January(yr1)-February(yr1) (DJF), and the influence of
206 the two events could extend until the summer of the following year. Therefore, we selected four
207 seasons from SON to June-July-August (JJA) in the following year for composite analysis in
208 this study. In addition, the year 1991 was excluded due to the strong eruption of Mount Pinatubo,
209 which had a large impact on the global carbon cycle (Mercado et al., 2009).

210

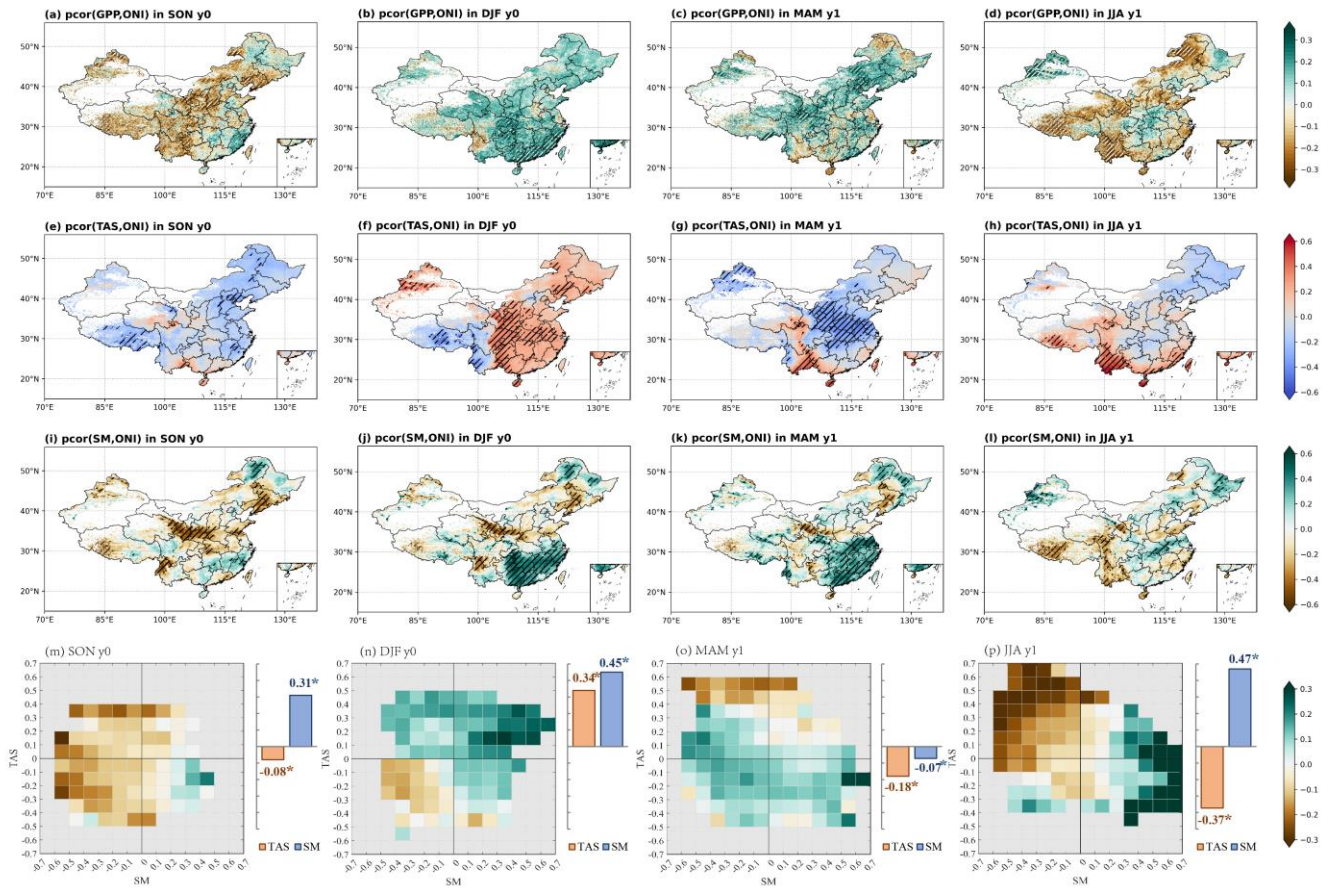
211 **Table 1.** Occurrences of ENSO and IOD events from 1981 to 2021.

Events	Years
El Niño	1982, 1986, 1987, 2002, 2009
La Niña	1984, 1988, 1999, 2007, 2011, 2020
pIOD	2019
nIOD	1992, 1996, 2016
El Niño & pIOD	1994, 1997, 2015
El Niño & nIOD	-
La Niña & pIOD	-
La Niña & nIOD	1998, 2010

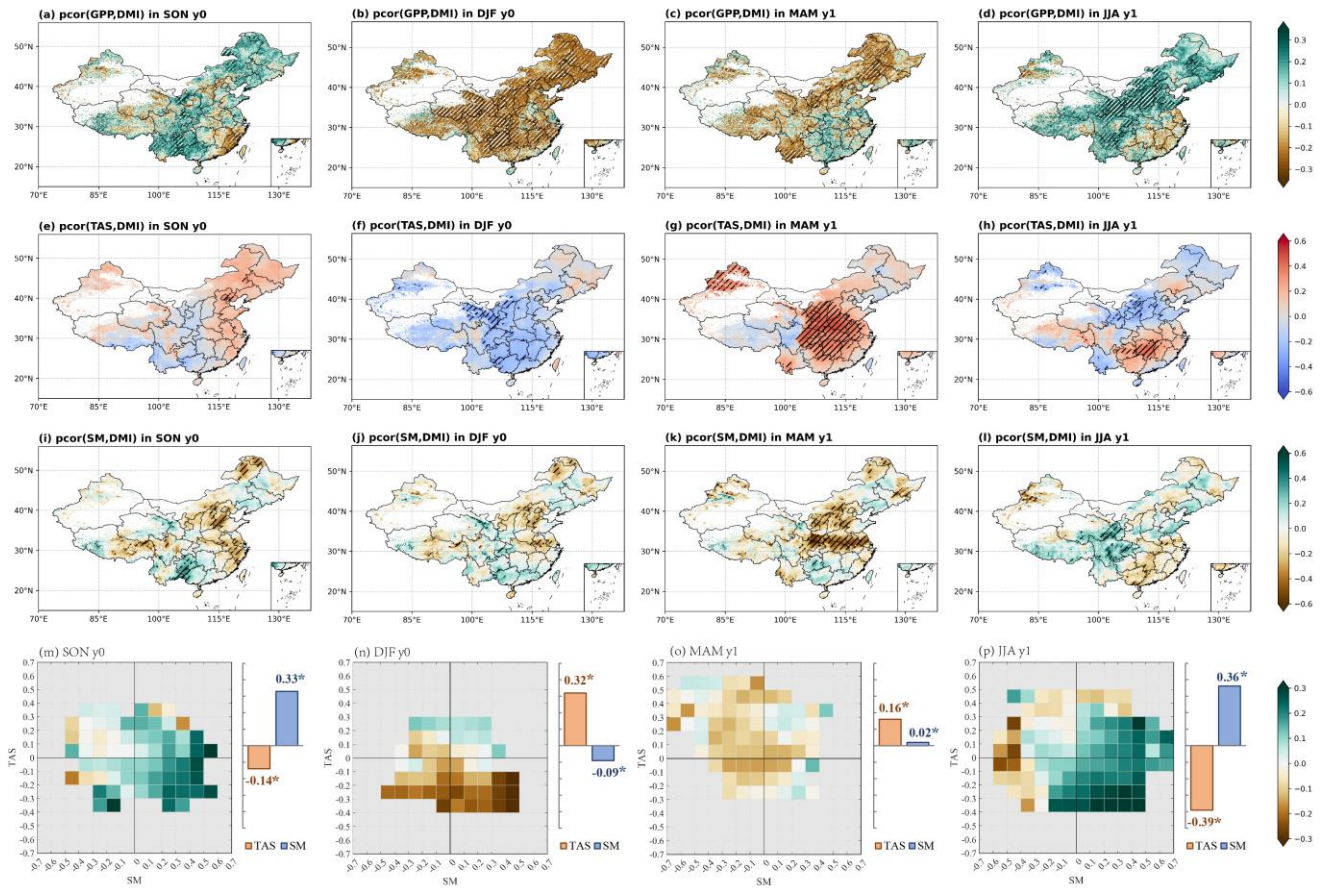
212

213 **3.Results**

214 **3.1 Historical relationship between GPP and ENSO**



215
 216 Fig. 2 Spatial patterns of partial correlation coefficients (*pcor*) between ONI and gross primary productivity
 217 (GPP) (a-d), surface air temperature (TAS) (e-h), soil moisture (SM) (i-l) in different seasons, controlling
 218 for the effect of DMI. Hatched areas represent significance at $p \leq 0.05$ based on the two-tailed Student's *t*-
 219 test. (m-p) Heatmaps represent the relationships of the *pcor* patterns among GPP, TAS, and SM, and bar
 220 charts illustrate the pattern correlations of these *pcor* values between GPP and TAS and SM on the national
 221 scale for each season. We here use seasonal average temperature as a mask to exclude regions with
 222 temperatures below zero, thereby minimizing the influence of phenology on GPP. Notably, asterisks (*) in
 223 the bar charts denote significance at $p < 0.05$.



224

225 Fig. 3 Same as Fig.2, but for DMI, controlling the effect of ONI.

226

227 We analyzed the *pcor* patterns between GPP and climate anomalies across different events
 228 using long time series data (Figs. 2 and 3). Following this, we calculated pattern correlation
 229 coefficients between the GPP and climate *pcor* patterns, aiming to investigate the varying
 230 impacts of key climate drivers (TAS and SM) on photosynthesis across different seasons (Figs.
 231 2m-p, and 3m-p).

232

233 Figure 2 reveals notable seasonal variations in the *pcor* patterns between GPP, related climate
 234 anomalies, and ONI index in December-January-February (DJF) when ENSO peaked,
 235 controlling the effect of DMI in September-October-November (SON) when IOD peaked.
 236 During SON, significant negative *pcor* between GPP and ONI is observed in regions including
 237 the Tibetan Plateau, Southwestern China, Loess Plateau, and Liaoning province (Fig. 2a).
 238 Clearly, this pattern aligns closely with the *pcor* pattern between soil moisture and ONI (Figs.

239 2a and i). The pattern correlation analysis between GPP and both TAS and SM underscores the
240 dominance of SM in influencing GPP anomalies, indicated by a correlation coefficient of 0.31
241 ($p < 0.05$). This finding suggests that the soil moisture deficit induced by El Niño largely
242 inhibits vegetation photosynthesis during this season (Fig. 2m).

243

244 Along with the peak of ENSO events in DJF, the *pcor* pattern between GPP and ONI exhibits
245 a distinct shift from the pattern in SON. Notably, DJF showcases significant positive *pcor*
246 values over large areas in southern China and weak positive *pcor* in the North and Northeastern
247 China (Fig. 2b). During this period, soil moisture still serves as a more influential factor in
248 driving GPP changes, reflected in a nation-wide pattern correlation coefficient of 0.45 ($p < 0.05$)
249 (Fig. 2n). Specifically, sufficient soil moisture during El Niño, coupled with higher winter
250 temperatures, contribute to a substantial enhancement in GPP across Southern China. In
251 contrast, the impact is weaker in the North and Northeast China due to the vegetation being in
252 the non-growing season, and localized soil water deficits (Figs. 2b, f, and j). In addition, GPP
253 experiences inhibition in some areas of southwestern China due to low temperatures and soil
254 drought.

255

256 Subsequently, the positive *pcor* of GPP decreases, or even turns slightly negative from DJF to
257 March-April-May (MAM) in southern China, primarily attributed to shifts of temperature (Figs.
258 2c and g). On a nationwide scale, temperature becomes the dominant factor in this period, but
259 it exhibits a negative correlation with GPP, with a spatial correlation coefficient of -0.18 ($p <$
260 0.5). This negative correlation is mainly due to negative GPP and positive temperature in the
261 southwest region, and positive GPP and negative temperature in the northern region (Figs. 2c
262 and 2g). Specifically, the negative *pcor* of GPP in southwest China is due to soil moisture
263 shortages (Fig. 2k). In the northern region, where a large area of croplands exists (Fig. S11),
264 human management practices may have a greater impact on GPP, particularly in the spring
265 when the growing season begins. However, these human management practices (e.g., irrigation,
266 fertilization, pesticide use) are not considered in the BEPS model, which could introduce

267 significant uncertainties in simulated GPP over cropland areas. Additionally, in some
268 grasslands of northern Hebei and parts of neighboring Inner Mongolia, GPP shows positive
269 *pcor* during El Niño events, possibly due to the strong legacy effects of climatic conditions in
270 DJF period.

271

272 Moving into JJA, the *pcor* of GPP exhibits widespread negative values again (Fig. 2d). In
273 general, during El Niño, increased soil moisture and lower temperatures greatly contribute to
274 enhanced GPP, while drier soil moisture and higher temperatures inhibit the increase in GPP
275 (Fig. 2p). Regionally, higher temperatures and lower soil moisture both contribute to the
276 negative GPP anomalies over southwestern China. However, lower soil moisture
277 predominantly curtails GPP over the Tibetan Plateau, the Yellow River basin, and northeastern
278 Inner Mongolia. Overall, the correlation coefficients between GPP and TAS and SM in summer
279 are comparable, with soil moisture exhibiting a slightly higher effect, represented by a
280 correlation coefficient of 0.47 ($p < 0.05$), compared to a correlation coefficient of -0.37 ($p <$
281 0.05) for temperature.

282

283 **3.2 Historical relationship between GPP and IOD**

284 In comparison, the *pcor* patterns between GPP and DMI in SON, controlling for the effect of
285 ONI, exhibit nearly opposite patterns to those between GPP and ONI (Figs. 2 and 3). In detail,
286 GPP demonstrates significant positive *pcor* values with DMI in southwestern China and eastern
287 Inner Mongolia, but displays significant negative *pcor* with DMI in southeastern China during
288 SON (Fig. 3a). In terms of climate drivers, during the pIOD events, for instance, wetter soil
289 and lower temperatures both benefit the significant enhancement in GPP in southwestern China,
290 while higher temperatures largely contribute to the enhancement in GPP over eastern Inner
291 Mongolia. Conversely, GPP is largely inhibited by the dry conditions in southeastern China
292 (Figs. 3e and i). Overall, soil moisture dominates the GPP anomaly in China, with a correlation
293 coefficient of 0.33 ($p < 0.05$) (Fig. 3m).

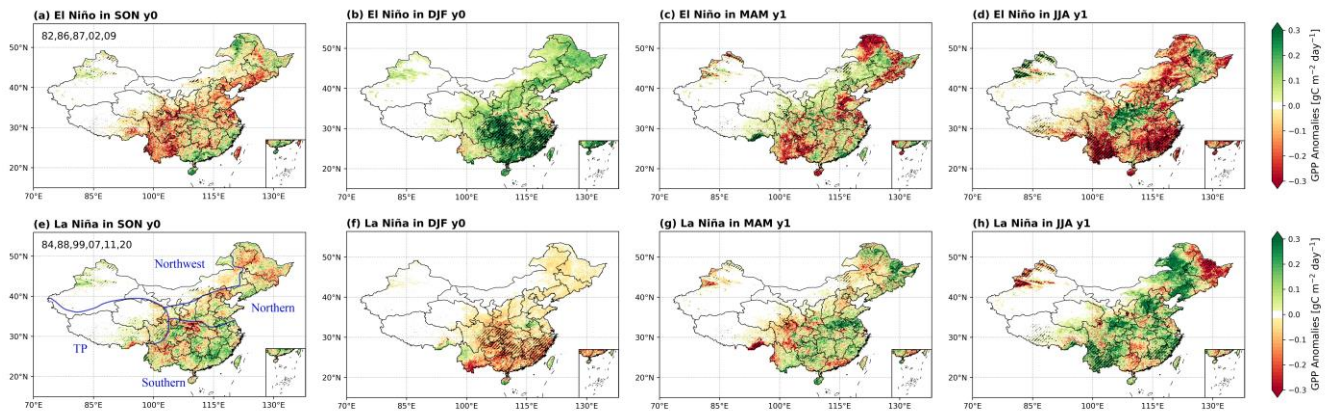
294 In DJF, GPP exhibits widespread significant negative *pcor* with DMI (Fig. 3b), primarily due
295 to the widespread negative *pcor* of temperature, characterized by a correlation coefficient of
296 0.32 ($p < 0.05$) (Figs. 3f and n). Moving into MAM, the significant negative *pcor* between GPP
297 and DMI carried on from those in DJF, but shifts to weak positive *pcor* in southeastern China,
298 driven by the significant positive *pcor* of temperature (Figs. 3c and g). However, the significant
299 negative *pcor* of soil moisture in the Jianghuai Basin and North China still negates the positive
300 effect of temperature (Fig. 3k). During this period, temperature remains the dominant factor,
301 with a nation-wide pattern correlation coefficient of 0.16 ($p < 0.05$) with GPP (Fig. 3o).

302

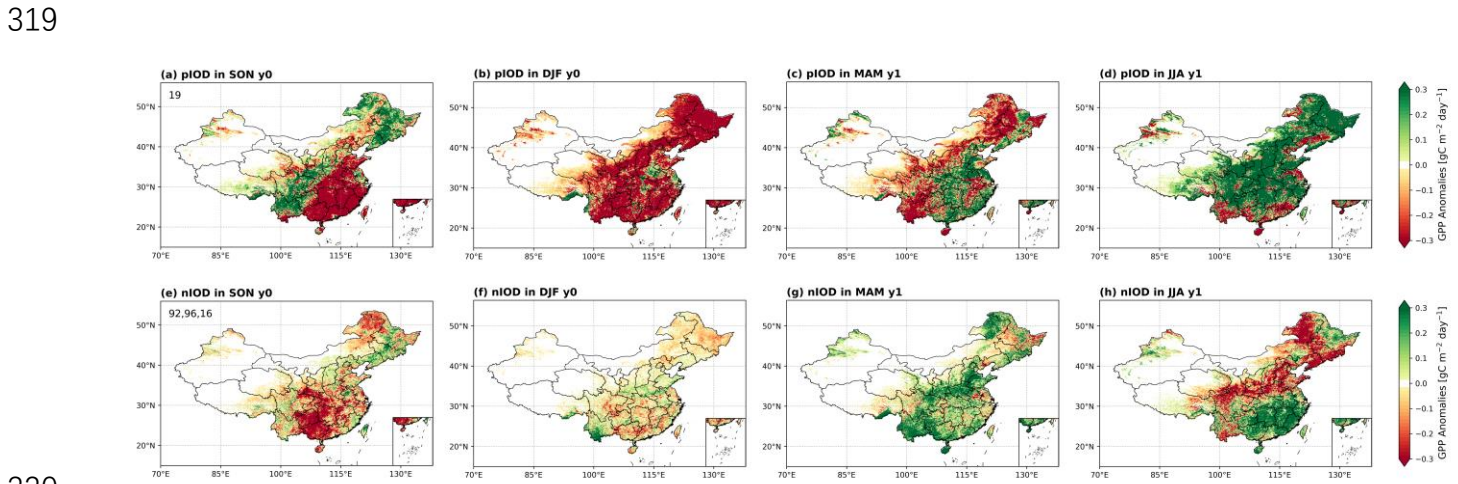
303 In JJA, the situation undergoes a change, showing the significant positive *pcor* of GPP over
304 southwestern, north and northeast China, and weak negative *pcor* over southeastern China (Fig.
305 3d). In other words, lower temperatures and gradually wetter soil are conducive to the increase
306 in vegetation photosynthesis, but heat and dry conditions cause the weak inhibition of
307 photosynthesis in southeastern China during the pIOD (Figs. 3p). However, unlike the ENSO
308 event, the role of temperature is slightly higher than that of SM in the IOD event, and the
309 correlations between GPP and TAS and SM are -0.39 and 0.36 ($p < 0.05$), respectively.

310

311 **3.3 GPP anomalies caused by specific ENSO and IOD events**



312
 313 Fig. 4. Spatial distributions of seasonal composite GPP anomalies for ENSO events, (a-d) for El Niño,
 314 and (e-h) for La Niña. The black slashes indicate areas where El Niño events differ significantly from
 315 La Niña events ($p \leq 0.05$) based on the Student's two-sample t -test. The two-digit year in first column
 316 denote the years used for composite analysis. Additionally, China is divided into four regions:
 317 Northwest China, Tibetan Plateau, Northern China, and Southern China, as shown in (e), which is used
 318 in the following context.



320
 321 Fig. 5. Similar to Fig. 4, but for spatial distributions of seasonal composite GPP anomalies for IOD
 322 events, (a-d) for pIOD, and (e-h) for nIOD. We did not conduct the significance test here owing to the
 323 limited samples.

324

325 While we have elucidated the historical relationship between GPP and ENSO and IOD events
326 through partial correlation coefficients and discussed the underlying climate drivers, we here
327 specifically selected actual events to conduct a composite analysis. This approach aims to
328 further comprehensive understanding of the effects of ENSO and IOD events on GPP variations
329 in China.

330

331 **3.3.1 ENSO-induced GPP anomalous patterns**

332 The impacts of El Niño and La Niña events exhibit opposite influences on GPP with obvious
333 seasonal variations (Fig. 4). Specifically, during SON, GPP anomalies are relatively weak,
334 indicating some suppressions over southwestern China and north China during El Niño events,
335 primarily attributed to dry conditions there (Figs. 4a and S4a). As ENSO peaks in DJF, GPP is
336 significantly strengthened during El Niño events and suppressed during La Niña events,
337 especially over southern China (Figs. 4b and f), aligning well with the patterns of *pcor* between
338 GPP and ONI, controlling the effect of DMI (Fig. 2b). Concurrently, the widespread higher
339 temperatures and wetter soil moisture both contribute to enhanced GPP over southern China
340 during El Niño events (Figs. S3b and S4b), while colder temperatures and drier soil moisture
341 lead to GPP suppression there during La Niña (Figs. 2f and 3f). In MAM as ENSO weakens
342 and vegetation starts to grow in the extratropics, the enhanced GPP over southern China in DJF
343 during El Niño events diminishes, even transitioning into a notable GPP reduction over
344 southwestern China, north China, and northeastern China (Fig. 4c). This transition is conspired
345 by phenological and climate changes including colder temperatures and prolonged dry
346 conditions (Figs. S3c and S4c). The GPP pattern exhibits the opposite transition in La Niña
347 (Fig. 4g). Moving to JJA, dry and hot conditions (Fig. S3d and S4d) lead to significant negative
348 GPP anomalies in southeastern and southwestern China in El Niño (Fig. 4d), whereas cool and
349 wet conditions result in positive GPP anomalies in La Niña events (Fig. 4h). Overall, GPP
350 anomalies induced by ENSO events in DJF and JJA are more pronounced than those in SON
351 and MAM, corresponding to the life cycle of event and vegetation growth periods, respectively.

352 Crucially, they demonstrate distinct GPP patterns, with significant enhancements in DJF and
353 reductions in JJA during El Niño events and reverse during La Niña events, aligning well with
354 the *pcor* pattern between GPP and ONI, controlling for the effect of DMI (Fig. 4). In addition,
355 the effect of ENSO on vegetation in southern China appears more substantial.

356

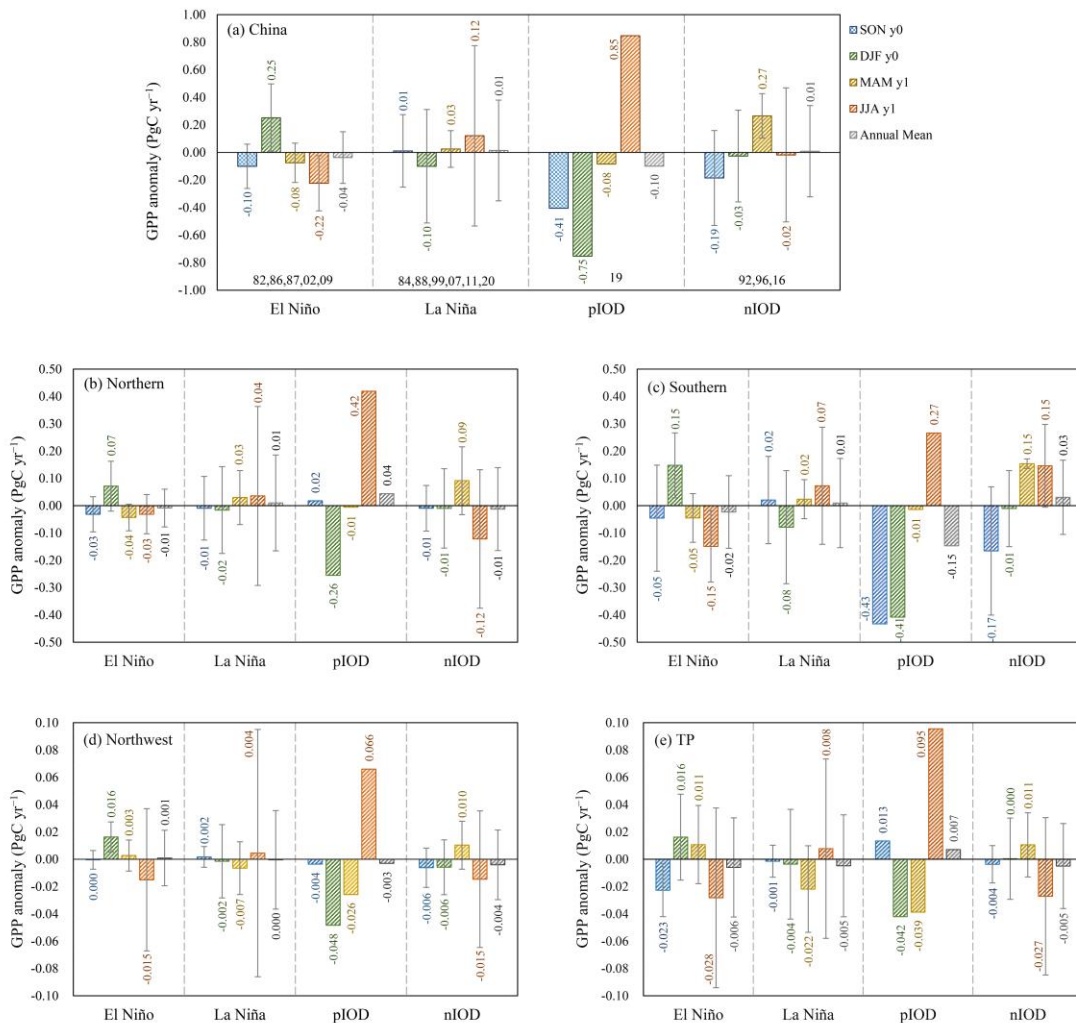
357 **3.3.2 IOD-induced GPP anomalous patterns**

358 During the period from 1981 to 2021, we only find one independent but extreme pIOD event
359 occurred in 2019 according to our criterion (Table 1). This extreme pIOD event extended from
360 June to December, a longer duration compared to other IOD events. Different from ENSO,
361 IOD basically peaks in SON. GPP anomalies induced by this extreme event align closely with
362 the long-term *pcor* patterns between GPP and DMI, controlling for the effect of ONI (Fig. 3).
363 Specifically, significant reductions in GPP occur in southeastern China in SON (Fig. 5a),
364 predominantly due to heat stress and severe drought conditions (Figs. S5a and S6a), consistent
365 with the findings revealed by Wang et al. (2021b). In DJF, the seasonal legacy of vegetation
366 state (Yan et al., 2023) and prolonged droughts lead to the widespread GPP reductions (Figs.
367 5b and S6b), outweighing the potential positive effect of higher temperatures (Fig. S5b). Of
368 course, the decline of GPP in southwestern China appears linked to lower temperatures (Figs.
369 5b and S5b). During MAM, the mitigation of soil moisture deficit and favorable higher
370 temperatures in southern China facilitate a shift in GPP from decline to increase (Fig. 5c). In
371 the north, persistent drought conditions notwithstanding (Fig. S6c), higher temperatures and
372 the onset of the growing season contribute to the enhanced GPP (Fig. 5c). In JJA, increased
373 precipitation over the Yangtze and Yellow River basins (Zhang et al., 2022) alleviates the soil
374 moisture deficits (Fig. S6d). Coupled with the relatively lower temperatures, this leads to
375 widespread GPP increases. Conversely, GPP suppressions in provinces south of 25°N and
376 around the Bohai Sea are attributed to higher temperatures and soil water deficits (Figs. 5d,
377 S5d, and S6d).

378

379 In contrast to the intense 2019 pIOD event, our composite analysis incorporates three weak
380 nIOD events, resulting in comparatively milder anomalies. In SON, different from pIOD event,
381 negative GPP anomalies in nIOD mainly appear in the provinces of Guizhou, Hunan, and
382 Guangxi (Fig. 5e), associated well with concurrent dry conditions (Fig. S6e). In DJF, although
383 the spatial pattern of soil moisture remains largely consistent with SON (Fig. S6f), a shift from
384 negative to positive temperature anomalies mitigates the evident GPP reductions (Fig. 5f). The
385 ongoing soil wetting and the onset of the growing season in northern hemisphere in MAM
386 result in the increased GPP over the Yellow River Basin and southwestern China (Figs. 5g, S5g,
387 and S6g). Subsequently, in JJA, the combination of wetter soil and lower temperatures
388 facilitates vegetation photosynthesis in southern China, while drier soil largely contributes to
389 the reduction in GPP in the north and northeastern China (Figs. 5h, S5h, and S6h).
390

391 **3.3.3 National and regional total GPP anomalies**



392
 393 Fig. 6. The seasonal and annual mean anomaly of GPP in different classified events for China (a), for
 394 Northern China (b), for Southern China (c), for Northwest China (d), and for Tibetan Plateau (e). The
 395 error bars show the standard deviation of different events in the composite analysis.

396
 397 We calculated the total GPP anomaly in China and various geographic regions for each
 398 classified event on both seasonal and annual scales (Fig. 6). Regionally, the geographical
 399 divisions include Northern China, Southern China, Northwest China, and Tibetan Plateau (Fig.
 400 4e). Notably, the North-South boundary aligns closely with the 0° isotherm in January and the
 401 annual precipitation line of 800 mm. The division between the North and the Northwest is

402 determined by the annual precipitation line of 400 mm, and the Tibetan Plateau is segmented
403 based on topographic factors.

404

405 In general, the GPP anomalies exhibit noticeable differences on the seasonal scale, while the
406 total annual anomalies do not show a significant magnitude due to the mutual offset of positive
407 and negative anomalies in different seasons. However, it is worth noting that our annual totals
408 are calculated from the SON in the developing year of the event to the JJA in the following
409 year. This method deviates from the traditional calendar year, and according to the conventional
410 definition of a “year”, the annual anomalies induced by these events can indeed be substantial.

411

412 Specifically, taking a national perspective (Fig. 6a), GPP anomalies during the El Niño and La
413 Niña events exhibit opposite signs in DJF and JJA, with greater magnitudes during these peak
414 periods of the events and the most vigorous growth period of vegetation, respectively. In terms
415 of the development process of the event, the annual anomaly of GPP is negative during El Niño,
416 with a magnitude of $-0.04 \pm 0.19 \text{ Pg C yr}^{-1}$, but positive during La Niña events, with a
417 magnitude of $0.01 \pm 0.37 \text{ Pg C yr}^{-1}$. The asymmetry of the positive and negative phases of IOD
418 is also evident in the total anomaly. For the pIOD event in 2019, GPP shows strong negative
419 anomalies with values of $-0.41 \text{ Pg C yr}^{-1}$ in SON and $-0.75 \text{ Pg C yr}^{-1}$ in DJF. Conversely, it
420 exhibits a marked positive anomaly in the following JJA, with a value of $0.85 \text{ Pg C yr}^{-1}$. The
421 annual total of GPP anomaly is opposite for pIOD and nIOD events, showing $-0.10 \text{ Pg C yr}^{-1}$
422 and $0.01 \pm 0.33 \text{ Pg C yr}^{-1}$, respectively. Moreover, large standard deviation indicated that there
423 are large uncertainties in the impact of different events, and each event has its uniqueness
424 (Capotondi et al., 2015).

425

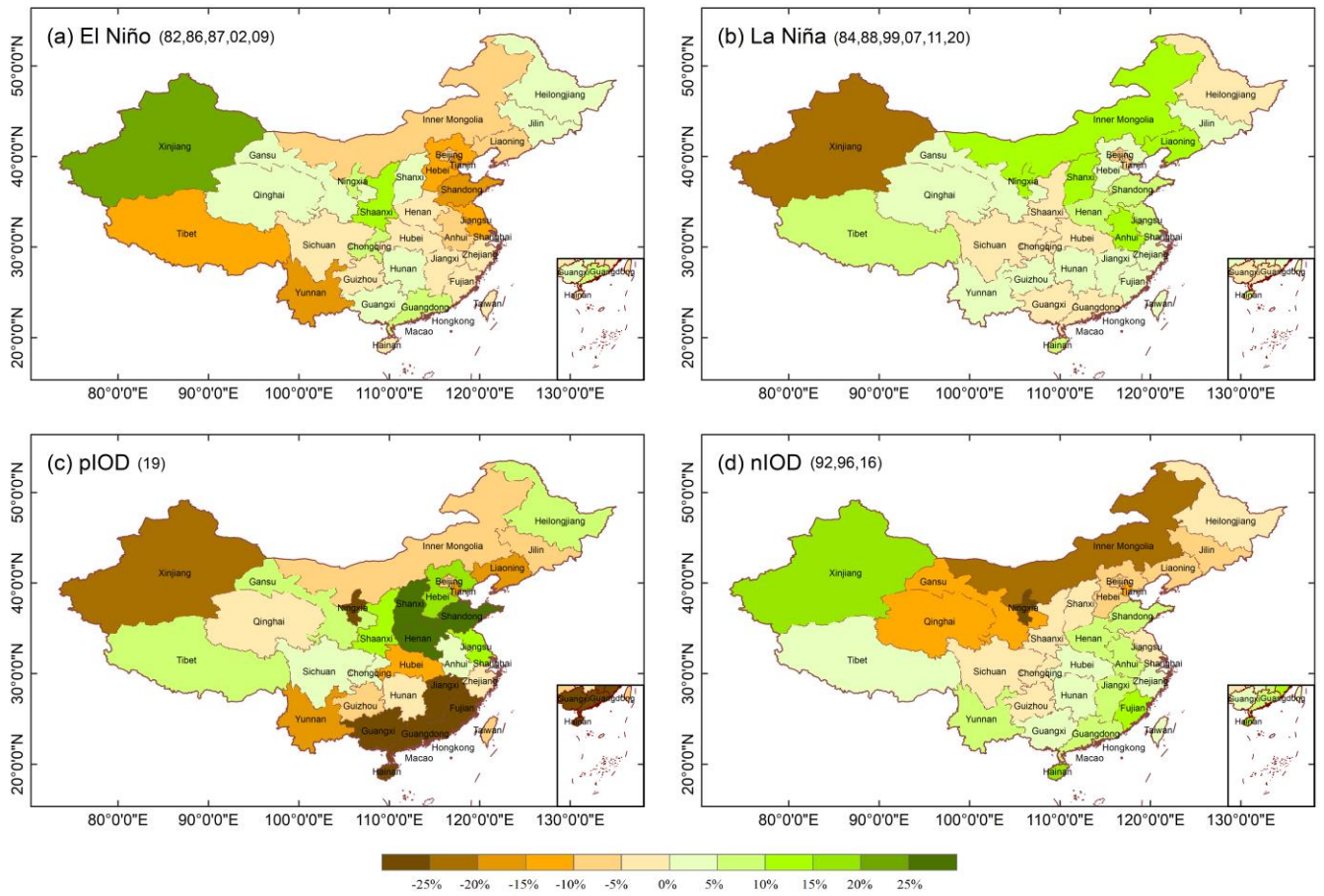
426 Additionally, the variation of GPP anomaly in each region is basically consistent with that at
427 the national scale, especially in the Southern. But regional differences indeed exist in the total
428 amount of GPP anomalies, demonstrating the difference in the impact of events on different
429 regions' GPP. Taking the 2019 extreme pIOD event as an example, the GPP showed a

430 significant negative anomaly in the Southern during the SON (Fig. 6c), resulting in negative
431 anomalies in GPP at the national scale (Fig. 6a), but weak positive anomalies in the Northern
432 and TP (Figs. 6b and e). Then, the GPP anomaly was close to zero in the Northern and Southern
433 in MAM (Figs. 6b and c), while it was still a significant negative anomaly in the Northwest
434 and TP (Figs. 6d and e). Moreover, the negative annual GPP anomalies in the Southern and
435 Northwest offset the positive anomalies of the TP and Northern, making a negative annual GPP
436 anomaly in the national of this event.

437

438 In terms of the magnitude of GPP anomalies, they are more pronounced in the Northern and
439 Southern regions, characterized by lush vegetation, mostly less than 0.5 Pg C yr^{-1} .
440 Meanwhile, GPP anomalies are relatively weaker in the Northwest and TP regions, primarily
441 covered by grassland, generally less than 0.1 Pg C yr^{-1} . Further, we calculate the contributions
442 of different regions to the national total GPP anomaly in each event (Table S3), referencing an
443 index described in the article by Ahlstrom et al. (2015), as detailed in the supplementary method.
444 Overall, the GPP anomaly in the Southern region dominates the national GPP variation,
445 contributing approximately 68% to ENSO events and 46% to IOD events, respectively. The
446 Northern GPP anomaly contributes approximately 28% to the national GPP variation in ENSO
447 events and 39% in IOD events. In addition, the contribution of GPP anomaly in the Northwest
448 and TP regions to the national GPP variation is within 10%.

449 **3.3.4 Relative changes in total GPP anomalies at provincial scale**



450

451 Fig. 7. Spatial distributions of relative changes of total composite anomalies of GPP at provincial scale

452 for different classified events.

453 We presented the spatial patterns of mean GPP anomalies from the SON in the developing year
454 to the JJA in the decaying year (Fig. S7) and further calculated provincial total GPP anomalies
455 (Fig. S8 and Table S3). Provinces with more extensive forest coverage, such as Yunnan, central
456 provinces housing the Qinling Mountains, and northeast provinces where the Greater and
457 Lesser Hinggan Mountains are situated, exhibit relatively larger provincial GPP anomalies.
458 However, differences are apparent among different events (Fig. S8). Considering differences
459 in area and vegetation coverage across provinces, our focus centers on the relative change of
460 GPP anomalies (Fig. 7). It's important to note that, due to different years used in composite
461 analysis, our quantitative comparisons are limited to the same event within different provinces,
462 while qualitative descriptions are extended to different events.

463

464 El Niño events generally induce substantial GPP changes in two main regions with a relative
465 change of over 10% (Fig. 7a). One region encompasses the northern coastal provinces,
466 including Tianjin, Hebei, Shandong, and Jiangsu, while the other is situated in the western part,
467 including Xinjiang, Tibet, and Yunnan provinces. Yunnan, rich in forest resources, bears the
468 brunt of El Niño's impact, exhibiting a total negative GPP anomaly of $-22.55 \text{ Tg C yr}^{-1}$ (Table
469 S4) and a relative change of approximately 16%. Despite comparable relative changes in GPP
470 for other provinces, their GPP anomalies are relatively smaller, within -5 Tg C yr^{-1} . Notably,
471 Xinjiang, characterized by a fragile forest steppe in the Altai and Tianshan Mountain regions,
472 consistently demonstrates substantial relative changes in GPP during both ENSO and other
473 events. Quantitatively, during the El Niño episode, Xinjiang witnesses a remarkable 24%
474 relative change in GPP, accompanied by a positive GPP anomaly of $-3.82 \text{ Tg C yr}^{-1}$. In contrast,
475 during the La Niña episode, provinces with notable relative changes are mainly concentrated
476 in the northern regions, such as Xinjiang, Inner Mongolia, Ningxia, Shanxi, and Liaoning
477 provinces (Fig. 7b). In addition, although the influence of ENSO on GPP in the southern China
478 is significant (Fig. 4), the total relative change through the year remains small due to the
479 cancellation of positive and negative anomalies in different seasons.

480 In the pIOD classification, only the 2019 extreme event is considered, resulting in the relative

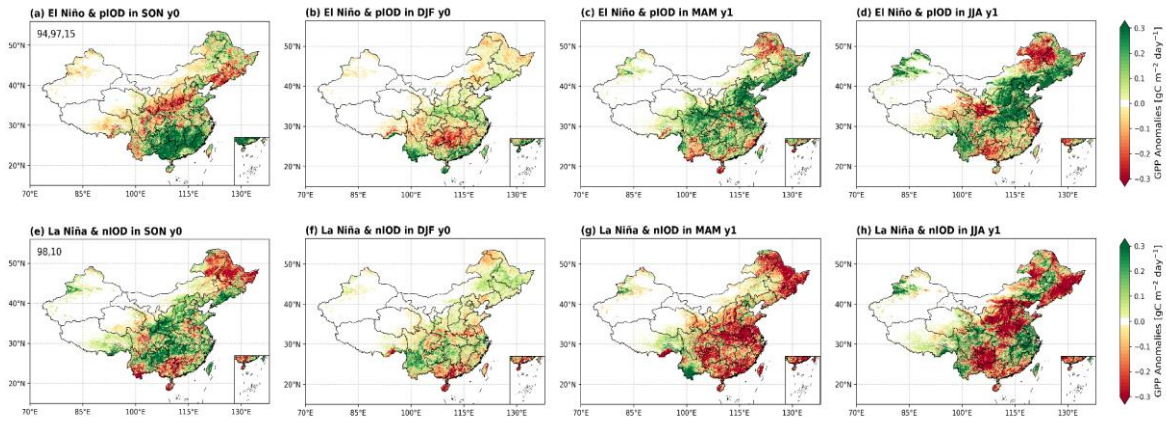
481 change in GPP anomalies exceeding 10% in approximately half of the provinces. Notably,
482 Jiangxi, Fujian, Guangxi, Guangdong, and Hainan experience reductions of more than 25% in
483 GPP, with Jiangxi exhibiting the largest GPP anomaly of $-31.50 \text{ Tg C yr}^{-1}$. Conversely,
484 Shandong, Shanxi, and Henan witness increase of over 25% in GPP (Fig. 7c). During nIOD
485 events, northern provinces generally exhibit negative relative changes, while southern
486 provinces display positive relative changes.

487

488 In summary, the relative changes in total GPP anomalies at the provincial scale exhibit an east-
489 west pattern in annual variation. Meanwhile, the influence of IOD events on GPP presents an
490 opposing north-south pattern.

491 **4. Discussion**

492 **4.1 The effect of compound ENSO and IOD events on China's GPP**



493

494 Fig. 8. Spatial distributions of seasonal composite GPP anomalies for compound events, (a-d) for El
495 Niño & pIOD events, and (e-h) for La Niña & nIOD events. The two-digit year in first column denote
496 the years used for composite analysis.

497

498 Indeed, despite IOD events being generally considered an independent coupled ocean-
499 atmosphere interaction (Saji et al., 1999), historical IOD events can occur in conjunction with
500 ENSO (Ham et al., 2017; Yang et al., 2015). These combined phenomena are most notable
501 represented by El Niño & pIOD and La Niña & nIOD events. Williams and Hanan (2011)
502 researched the interactive effects of ENSO and IOD on African GPP, relying on an offline
503 terrestrial biosphere model simulation. Their findings suggested that IOD could cause obvious
504 anomalous GPP over much of Africa, capable of suppressing or even reversing ENSO signals
505 in GPP anomalies. In addition, Yan et al. (2023) explored the interactive effects of ENSO and
506 IOD on seasonal anomalies of tropical net land carbon flux using the TRENDYv9 multi-model
507 simulations, revealing diverse effects in different sub-continent and seasons. We explore the
508 anomalies of GPP in compound events based on composite analysis (Fig. 8), and the spatial
509 patterns of soil moisture and temperature anomalies are shown in the appendix (Figs. S9 and
510 S10).

511 The spatial patterns of the GPP anomalies during concurrent ENSO and IOD events differ from
512 those in single events, although some similarities are evident. We observed that GPP anomalies
513 during El Niño & pIOD events are generally opposite to those during La Niña & nIOD events.
514 Here, we focus on the impacts of El Niño & pIOD events. In El Niño & pIOD events, GPP
515 anomalies exhibit a general opposition, with enhanced vegetation photosynthesis in the
516 southern regions and inhibited in the northern regions during SON. During El Niño & pIOD
517 events, photosynthesis generally increased in the southern regions and decreased in the
518 northern regions during SON, indicating opposing GPP anomalies across these areas. This
519 spatial characteristic of GPP anomalies bears some resemblance to that induced by El Niño
520 alone (Figs. 4a and 8a). Weak GPP anomalies are generally observed in DJF, with noticeable
521 negative GPP anomalies in Guizhou and Hunan, and some positive GPP anomalies in regions
522 south of 25°N (Fig. 8b). Notably during DJF, while significant positive GPP anomalies occur
523 in El Niño events (Fig. 4b), simultaneous pIOD events induce significant negative GPP
524 anomalies (Fig. 5b). When both events coincide, their impacts seem to largely counterbalance
525 each other, resulting in a more neutral GPP anomaly. In MAM, GPP increases in Northern
526 China (Fig. 8c). Subsequently, in JJA, vegetation photosynthesis experiences a significant
527 increase in the Northern and Yunnan provinces (Fig. 8d).

528 It is worth noting that the impacts of compound events on China's GPP may not follow a
529 straightforward linear superposition of the effects of two individual events. While their effects
530 are nearly opposite when occurring separately, the positive and negative effects on GPP may
531 be not simply cancelled each other out when they coincide. This complexity arises from the
532 simultaneous occurrence of two tropical air-sea interaction modes, leading to intricate effects
533 on mid-latitude circulations. Given the limited number of compound events, further exploration
534 is necessary to unravel the effects of ENSO and IOD on GPP in China.

535 **4.2 Modulation of large-scale circulations on China's GPP**

536 China's GPP is intricately influenced by atmospheric circulations and sea surface temperature
537 (Li et al., 2021; Ying et al., 2022). Ying et al. (2022) showed significant correlations between

538 seasonal GPP variation in China and climate phenomena such as ENSO, Pacific Decadal
539 Oscillation (PDO), and Arctic Oscillation (AO), based on the Residual Principal Component
540 analysis. Their research indicated that these identified SST and circulation factors could
541 account for 13%, 23% and 19% of the seasonal GPP variations in spring, summer and autumn,
542 respectively. And Li et al. (2021) proved that GPP response to El Niño varied with PDO phases
543 during the growing seasons of typical El Niño years. Although both studies emphasized the
544 impact of ENSO on China's GPP and explored the roles of PDO and AO, the IOD was notably
545 absent from their analyses. Contrastingly, our study sheds light on the significant influence of
546 the extreme positive phase of IOD in 2019, showing a substantial negative GPP anomaly in
547 southeastern China during SON, aligning with findings by Wang et al. (2021b). Moreover, the
548 integration of partial correlation and composite analysis in our study elucidates the
549 considerable impact of IOD on China's GPP within this context. Importantly, our research
550 underscores the temporal and spatial variability in the effects of IOD and ENSO on GPP across
551 different seasons and regions. This complexity in ocean–atmosphere teleconnections implies
552 that other climate oscillations, such as Polar/Eurasia and Atlantic Multidecadal Oscillation
553 (AMO), might also contribute to influencing China's GPP (Zhu et al., 2017).

554 **4.3 Uncertainties in BEPS Simulations**

555 The simulation of China's GPP by BEPS is subject to several sources of uncertainty inherent
556 in the model's structure, parameterizations, processes, and input data (Chen et al., 2012; Chen
557 et al., 2017; He et al., 2021a; Liu et al., 2018; Wang et al., 2021a). Leaf Area Index (LAI), a
558 crucial input for the BEPS model, is derived from global remote sensing data that inherently
559 possess uncertainties in spatial distribution and trend changes. Previous studies have
560 highlighted significant uncertainties in simulating carbon budget of global terrestrial
561 ecosystems when employing different LAI remote sensing data (Chen et al., 2019; Liu et al.,
562 2018). Foliage clumping index which is used to separate sunlit and shaded LAI can also cause
563 some uncertainties in simulating GPP, because the current version of BEPS used the time-
564 invariant satellite-derived clumping index (Chen et al., 2012). Biases in meteorological drivers,

565 such as precipitation, can further result in considerable uncertainties in simulating terrestrial
566 carbon cycle. The choice of precipitation products, for instance, has been shown to yield
567 considerable differences in simulated net land-atmosphere carbon flux (Wang et al., 2021c).
568 Moreover, BEPS model, like other terrestrial biosphere models, lacks consideration for
569 vegetation adaptability to rising CO₂ concentration, potentially leading to an overestimation of
570 the fertilization effect on GPP. In addition, the accuracy of simulations over agricultural areas
571 is compromised in BEPS, as it only considers crops with a C3 photosynthetic pathway and
572 overlooks C4 crops (He et al., 2017; He et al., 2021b; Ju et al., 2006). Although BEPS simulated
573 GPP demonstrates relatively high consistency with the measured GPP of Yingke Station (CRO),
574 located in the northwest of China, its accuracy lacks validation over the extensive farmlands in
575 north and northeastern China where various crops are grown (Fig. S11). Agricultural operations,
576 particularly irrigation, which can significantly impact GPP, are not considered in BEPS. He et
577 al. (2021a) revealed extensive wetting signals over croplands in arid and semi-arid areas which
578 exerted strong impacts on GPP and evapotranspiration simulations in BEPS after assimilating
579 the Soil Moisture Active Passive (SMAP) soil moisture product. Furthermore, photosynthetic
580 key parameters, such as carboxylation capacity at 25°C ($V_{\text{cmax},25}$), can largely determine the
581 performance in simulating GPP. After assimilating the solar-induced chlorophyll fluorescence
582 (SIF) from the Orbiting Carbon Observing Satellite-2 (OCO-2) to optimize $V_{\text{cmax},25}$ of different
583 plant functional types (PFTs) in BEPS, previous studies suggested the improvements in
584 simulating GPP at regional and global scales to some extent (He et al., 2019; Wang et al.,
585 2021a).

586 **4.4 Limitations and Future work**

587 While the seasonal legacy effects of climate on subsequent vegetation have been widely
588 confirmed (Bastos et al., 2020; Bastos et al., 2021), they were not fully accounted for in this
589 study. During ENSO and IOD events, temperature and soil moisture vary with seasons,
590 resulting in diverse conditions such as high temperature and drought, high temperature and wet,
591 low temperature and drought, and low temperature and wet across different regions and seasons.

592 Vegetation does not immediately respond to changes in climatic condition changes due to its
593 environmental resistance and self-regulation. These legacy effects are complex and vary by
594 region as ENSO or IOD events progress through different seasons.

595 Spring serves as a transitional period between the peak of the climatic event and the peak of
596 the growing season, making it challenging to fully explain the spatial patterns of GPP anomalies
597 in parts of northern China based on temperature and soil moisture. Higher temperatures during
598 DJF in El Niño events (Fig. 2f) can advance the growing season, subsequently impacting
599 vegetation in the following spring. Sanders-DeMott et al. (2020) have proved that a warm
600 winter can enhance the photosynthetic capacity of vegetation in the subsequent spring.
601 Additionally, Yan et al. (2023) quantified the influence of the preceding and contemporaneous
602 climatic conditions on NEP during the 1997/98 El Niño and pIOD compound event, showing
603 that legacy effects can counteract or even reverse the effects of contemporaneous climatic
604 conditions.

605 Additionally, Temperature and water (precipitation or soil moisture) have long been regarded
606 as the main climate factors driving inter-annual fluctuations of GPP or NEP (Zeng et al., 2005;
607 Piao et al., 2013; Ahlstrom et al., 2015; Wang et al., 2016; Jung et al., 2017; Humphrey et al.,
608 2018). However, other factors, such as VPD and radiation, also play important roles. This may
609 explain the occasional mismatch between GPP patterns and TAS/SM in certain regions in Figs.
610 2 and 3. Overall, although the dominant driving factors vary seasonally, TAS and SM capture
611 GPP variations more effectively on a national scale.

612 Finally, it is worth noting that climate factors often interact closely with one another. For
613 example, soil moisture can influence changes in surface air temperature, and vice versa. As a
614 result, in addition to direct effects, climate drivers may also impact vegetation through indirect
615 pathways. Humphrey et al. (2021) discussed the direct and indirect effects of soil moisture on
616 variations in terrestrial interannual carbon sinks—specifically, through its influence on
617 temperature and vapor pressure deficit (VPD)—using simulations from four Earth System
618 Models. This area of interaction warrants further investigation in future research.

619 5. Conclusion

620 In this paper, we used partial correlation coefficients and composite analysis to investigate the
621 impacts of ENSO and IOD events on China's GPP during 1981–2021. The partial correlation
622 results reveal that the effects of ENSO and IOD on GPP and related climate in China exhibit
623 distinct seasonal variations and are basically opposite. Specifically, during SON, significant
624 negative *pcor* between GPP and ENSO is observed over the Tibetan Plateau, southwestern
625 China, Loess Plateau, and Liaoning. In DJF, strongly positive *pcor* occurs over southern China,
626 weakening in the subsequent MAM, albeit with some enhancements in northern Hebei and
627 neighboring Inner Mongolia. The *pcor* then turns generally negative in JJA. In contrast,
628 significant positive *pcor* between GPP and IOD is noted in southwestern and Northeast China
629 during SON. Subsequently, widespread negative *pcor* appears during DJF, persisting
630 significantly in most western and northern regions during MAM. In JJA, the *pcor* becomes
631 significantly positive in southwestern, north and northeast China. Moreover, the correlation
632 coefficients between GPP and climate show that GPP anomalies are primarily dominated by
633 SM during ENSO events except MAM, while temperature generally plays a more important
634 role during IOD events except SON.

635

636 The composite analysis results validate the patterns of GPP anomalies observed in the partial
637 correlation. Generally, China's annual total GPP demonstrates modest positive anomalies in La
638 Niña and nIOD years, contrasting with minor negative anomalies in El Niño and pIOD years.
639 This results from the counterbalancing effects, with significantly greater GPP anomalous
640 magnitudes in DJF and JJA. Regionally, GPP anomalies fluctuate more in the Southern and
641 Northern regions. The GPP anomaly in the Southern region dominates the national GPP
642 variation, with the contribution of 68% to ENSO events and 46% to IOD events, respectively.
643 On the provincial scale, western and northern provinces in experience larger relative annual
644 variations during ENSO events, with magnitudes exceeding 10%, exhibiting a general east-
645 west pattern. Conversely, provinces in the southern and Northern China witness larger relative

646 changes during IOD events, showing an opposing north-south pattern. For instance, the 2019
647 extreme pIOD led to relative changes of over 25% in certain provinces in the south and north.
648

649 **Author contributions**

650 Jun Wang designed the experiments. Ran Yan processed the data, carried out the analysis and wrote the
651 original manuscript. All the authors contributed to the writing of the paper.

652 **Acknowledgement**

653 The calculations in this paper have been done on the computing facilities in the High Performance
654 Computing Center (HPCC) of Nanjing University. This study was supported by the Natural Science
655 Foundation of China (Grants 42141005 and 42475129), and the Natural Science Foundation of Jiangsu
656 Province, China (BK20221449).

657 **Conflict of Interest**

658 The authors declare no competing interests.

659 **Data Availability**

660 ERA5 meteorological data are available at <https://cds.climate.copernicus.eu/cdsapp#!/dataset/reanalysis-era5-single-levels?tab=overview>. The remote-sensing GLOBMAP LAI data is available at
661 <https://zenodo.org/record/4700264#.YzvSYnZBxD8/>. The carbon dioxide emissions data is available
662 at https://gml.noaa.gov/webdata/ccgg/trends/co2/co2_mm_mlo.txt. Vegetation type data for B
663 EPS simulations is obtained from <https://lpdaac.usgs.gov/products/mcd12q1v006/>. Soil texture data
664 is available at <https://data.tpdc.ac.cn/zh-hans/data/611f7d50-b419-4d14-b4dd-4a944b141175>. Soil
665 moisture and surface air temperature from ERA5-Land are available at <https://cds.climate.copernicus.eu/cdsapp#!/dataset/reanalysis-era5-land-monthly-means?tab=overview>. Sea surface temperature
666 dataset from ERSSTv5 is available at <https://psl.noaa.gov/data/gridded/data.noaa.ersst.v5.html>. Eight sites of the ten are from ChinaFlux (<http://www.chinaflux.org/enn/index.aspx>), and
669 <http://www.chinaflux.org/enn/index.aspx>, and

670 two are from National Tibetan Plateau Third Pole Environment (<http://data.tpdc.ac.cn/zh-hans>).
671 FluxSat GPP Version 2.2 are available at https://avdc.gsfc.nasa.gov/pub/tmp/FluxSat_GPP.

672

673 **Reference**

674 Ahlstrom, A., Raupach, M. R., Schurgers, G., Smith, B., Arneeth, A., Jung, M., Reichstein, M., Canadell,
675 J. G., Friedlingstein, P., Jain, A. K., Kato, E., Poulter, B., Sitch, S., Stocker, B. D., Viovy, N., Wang,
676 Y. P., Wiltshire, A., Zaehle, S., Zeng, N.: The dominant role of semi-arid ecosystems in the trend and
677 variability of the land CO₂ sink, *Science*, 348(6237), 895-899, <https://doi:10.1126/science.aaa1668>,
678 2015.

679 Antonietta, C., Andrew, T., Matthew, N., Emanuele, Di., Jin-Yi, Y., Pascale, B., Julia, C., Boris, D.,
680 Benjamin G., Eric, G., Fei-Fe, J., Kristopher, K., Benjamin, K., Tong, L., Niklas, S., Yan, X., and Sang-
681 Wook, Y.: Understanding ENSO Diversity, *B. Am. Meteorol. Soc.*, 96(6), 921-938,
682 <https://doi:10.1175/BAMS-D-13-00117.1>, 2015.

683 Bastos, A., Ciais, P., Friedlingstein, P., Sitch, S. and Zaehle, S.: Direct and seasonal legacy effects of
684 the 2018 heat wave and drought on European ecosystem productivity. *Sci. Adv.*, 6, eaba2724,
685 <https://doi.org/10.1126/sciadv.aba2724>, 2020.

686 Bastos, A., Orth, R., Reichstein, M., Ciais, P., Viovy, N., Zaehle, S., Anthoni, P., Arneeth, A., Gentine, P.,
687 Joetzjer, E., Lienert, S., Loughran, T., McGuire, P. C., O, S., Pongratz, J., and Sitch, S.: Vulnerability of
688 European ecosystems to two compound dry and hot summers in 2018 and 2019, *Earth Syst. Dynam.*,
689 12, 1015–1035, <https://doi.org/10.5194/esd-12-1015-2021>, 2021.

690 Bauch, M.: Chapter 15 - Impacts of extreme events on medieval societies: Insights from climate history,
691 in: *Climate Extremes and Their Implications for Impact and Risk Assessment*, edited by: Sillmann, J.,
692 Sippel, S., and Russo, S., Elsevier, 279-291, <https://doi.org/10.1016/B978-0-12-814895-2.00015-X>,
693 2020.

694 Chen, J., Liu, J., Cihlar, J., and Goulden, M.: Daily canopy photosynthesis model through temporal and
695 spatial scaling for remote sensing applications, *Ecol. Model.*, 124, 99–119, [https://doi:10.1016/S0304-](https://doi:10.1016/S0304-3800(99)00156-8)
696 3800(99)00156-8, 1999.

697 Chen, J. M., Mo, G., Pisek, J., Liu, J., Deng, F., Ishizawa, M., and Chan, D.: Effects of foliage clumping
698 on the estimation of global terrestrial gross primary productivity, *Global Biogeochem. Cy.*, 26, GB1019,
699 <https://doi.org/10.1029/2010GB003996>, 2012.

700 Chen, J., Ju, W., Ciais, P., Viovy, N., Liu, R., Liu, Y., and Lu X.: Vegetation structural change since 1981
701 significantly enhanced the terrestrial carbon sink, *Nat. Commun.*, 10, 4259, [https://doi:10.1038/s41467-](https://doi:10.1038/s41467-019-12257-8)
702 019-12257-8, 2019.

703 Chen, Z., Chen, J., Zhang, S., Zheng, X., Ju, W., Mo, G., Lu, X.: Optimization of Terrestrial Ecosystem
704 Model Parameters Using Atmospheric CO₂ Concentration Data With the Global Carbon Assimilation
705 System (GCAS), *J. GEOPHYS. RES. - BIOGEO.*, 122, 3218-3237,
706 <http://doi.org/10.1002/2016JG003716>, 2017.

707 Gough, C.: Terrestrial primary production: Fuel for life, *Nature Education Knowledge*, 3. 2012

708 Ham, Y., Choi, J., and Kug, J.: The weakening of the ENSO–Indian Ocean Dipole (IOD) coupling
709 strength in recent decades, *Clim. Dynam.*, 49(1), 249-261, <https://doi:10.1007/s00382-016-3339-5>,
710 2017.

711 He, B., Chen, C., Lin, S., Yuan, W., Chen, H., Chen, D., Zhang, Y., Guo, L., Zhao, X., Liu., Piao, S.,
712 Zhong, Z., Wang, R., and Tang, R.: Worldwide impacts of atmospheric vapor pressure deficit on the
713 interannual variability of terrestrial carbon sinks, *Natl. Sci. Rev.*, 9(4), nwab150,
714 <https://doi:10.1093/nsr/nwab150>, 2022.

715 He, L., Chen, J., Liu, J., Bélair, S., and Luo, X.: Assessment of SMAP soil moisture for global simulation
716 of gross primary production, *J. Geophys. Res. – Biogeo.*, 122(7), 1549-1563,
717 <https://doi:10.1002/2016jg003603>, 2017.

718 He, L., Chen, J., Liu, J., Zheng, T., Wang, R., Joiner, J., Chou, S., Cheng, B., Liu, Y., and Liu, R.:
719 Diverse photosynthetic capacity of global ecosystems mapped by satellite chlorophyll fluorescence
720 measurements, *Remote Sens. Environ.*, 232, <https://doi:10.1016/j.rse.2019.111344>, 2019.

721 He, L., Chen J., Mostovoy, G., and Gonsamo, A.: Soil Moisture Active Passive Improves Global Soil
722 Moisture Simulation in a Land Surface Scheme and Reveals Strong Irrigation Signals Over Farmlands,
723 *Geophys. Res. Lett.*, 48(8), <https://doi:10.1029/2021gl092658>, 2021a.

724 He, L., Wang, R., Mostovoy, G., Liu, J., Chen, J., Shang, J., Liu, J., McNairn, H., and Powers, J.: Crop

725 Biomass Mapping Based on Ecosystem Modeling at Regional Scale Using High Resolution Sentinel-2
726 Data, *Remote Sens.*, 13(4), <https://doi:10.3390/rs13040806>, 2021b.

727 He, Q., Ju, W., Dai, S., He, W., Song, L., Wang, S., Li, X., and Mao, G.: Drought Risk of Global
728 Terrestrial Gross Primary Productivity Over the Last 40 Years Detected by a Remote Sensing-Driven
729 Process Model. *J. Geophys. Res. – Biogeo.*, 126(6), <https://doi.org/10.1029/2020JG005944>, 2021.

730 Hersbach, H., Bell, B., Berrisford, P., Biavati, G., Horányi, A., Muñoz Sabater, J., Nicolas, J., Peubey,
731 C., Radu, R., Rozum, I., Schepers, D., Simmons, A., Soci, C., Dee, D., Thépaut, J-N.: ERA5 hourly
732 data on single levels from 1940 to present, Copernicus Climate Change Service (C3S) Climate Data
733 Store (CDS) [data set], <https://doi:10.24381/cds.adbb2d47>, 2023.

734 Houghton, R. A.: Balancing the global carbon budget, *Annu. Rev. Eart. Pl. Sc.*, 35, 313-347,
735 <https://doi:10.1146/annurev.earth.35.031306.140057>, 2007.

736 Humphrey, V., Zscheischler, J., Ciais, P., Gudmundsson, L., Sitch, S., and Seneviratne, SI.: Sensitivity
737 of atmospheric CO₂ growth rate to observed changes in terrestrial water storage, *Nature*, 560(7720),
738 628-631, <https://doi.org/10.1038/s41586-018-0424-4>, 2018.

739 Humphrey, V., Berg, A., Ciais, P., Gentine, P., Jung, M., Reichstein, M., Seneviratne, SI., and
740 Frankenberg, C.: Soil moisture–atmosphere feedback dominates land carbon uptake variability, *Nature*,
741 592(7852), 65-69, <https://doi.org/10.1038/s41586-021-03325-5>, 2021.

742 Jung, M., Reichstein, M., Schwalm, C. R., Huntingford, C., Sitch, S., Ahlstrom, A., Arneth, A., Camps-
743 Valls, G., Ciais, P., Friedlingstein, P., Gans, F., Ichii, K., Ain, A., Kato, E., Papale, D., Poulter, B., Raduly,
744 B., Rödenbeck, C., Tramontana, G., Viovy, N., Wang, YP., Weber, U., Zaehle, S., and Zeng, N.:
745 Compensatory water effects link yearly global land CO₂ sink changes to temperature, *Nature*, 541(7638),
746 516-520, <https://doi.org/10.1038/nature20780>, 2017.

747 Joiner, J., Yoshida, Y., Zhang, Y., Duveiller, G., Jung, M., Lyapustin, A., Wang, Y., and Tucker, C. J.:
748 Estimation of Terrestrial Global Gross Primary Production (GPP) with Satellite Data-Driven Models
749 and Eddy Covariance Flux Data, *Remote Sens.*, 10(9), <https://doi:10.3390/rs10091346>, 2018.

750 Ju, W., Chen J., Black T., Barr, A., Liu, J., and Chen, B.: Modelling multi-year coupled carbon and
751 water fluxes in a boreal aspen forest, *Agr. Forest Meteorol.*, 140(1-4), 136-151,
752 <https://doi:10.1016/j.agrformet.2006.08.008>, 2006.

753 Fischer, G., Nachtergaele, F., Prieler, S., van Velthuisen, H. T., Verelst, L., Wiberg, D.: Global Agro-
754 ecological Zones Assessment for Agriculture (GAEZ 2008), IIASA [data set], Laxenburg, Austria and
755 FAO, Rome, Italy, 2008.

756 Friedl, M., Sulla-Menashe, D.: MCD12Q1 MODIS/Terra+Aqua Land Cover Type Yearly L3 Global
757 500m SIN Grid V006, NASA EOSDIS Land Processes Distributed Active Archive Center [data set],
758 2019.

759 Kim, J., Kug J., and Jeong S.: Intensification of terrestrial carbon cycle related to El Niño-Southern
760 Oscillation under greenhouse warming, *Nat. Commun.*, 8, <https://doi:10.1038/s41467-017-01831-7>,
761 2017.

762 Lan, X., Tans, P. and K.W. Thoning: Trends in globally-averaged CO₂ determined from NOAA Global
763 Monitoring Laboratory measurements [data set], <https://doi.org/10.15138/9N0H-ZH07>, 2022.

764 Li, X., Cheng, G., Liu, S., Xiao, Q., Ma, M., Jin, R., Che, T., Liu, Q., Wang, W., Qi, Y., Wen, J., Li, H.,
765 Zhu, G., Guo, J., Ran, Y., Wang, S., Zhu, Z., Zhou, J., Hu, X., Xu, Z.: Heihe watershed allied telemetry
766 experimental research (HiWATER): scientific objectives and experimental design. *Bull. Am. Meteorol.*
767 *Soc.* 94 (8), 1145–1160, <https://doi.org/10.1175/BAMS-D-12-00154.1>, 2013.

768 Li, Y., Dan, L., Peng, J., Wang, J., Yang, F., Gao, D., Yang, X., and Yu, Q.: Response of Growing Season
769 Gross Primary Production to El Niño in Different Phases of the Pacific Decadal Oscillation over Eastern
770 China Based on Bayesian Model Averaging, *Adv. Atmos. Sci.*, 38(9), 1580-1595,
771 <https://doi:10.1007/s00376-021-0265-1>, 2021.

772 Liu, J., Chen J., Cihlar, J., and Park W.: A process-based boreal ecosystem productivity simulator using
773 remote sensing inputs, *Remote Sens. Environ.*, 62(2), 158-175, [https://doi.org/10.1016/S0034-](https://doi.org/10.1016/S0034-4257(97)00089-8)
774 [4257\(97\)00089-8](https://doi.org/10.1016/S0034-4257(97)00089-8), 1997.

775 Liu, Y., Liu, R., and Chen, J.: Retrospective retrieval of long-term consistent global leaf area index
776 (1981-2011) from combined AVHRR and MODIS data. *J. Geophys. Res. Biogeosci.* 117 (G4), G04003,
777 <https://doi.org/10.1029/2012JG002084>, 2012.

778 Liu, Y., Xiao, J., Ju, W., Zhu, G., Wu, X., Fan, W., Li, D., and Zhou, Y.: Satellite-derived LAI products
779 exhibit large discrepancies and can lead to substantial uncertainty in simulated carbon and water fluxes,
780 *Remote Sens. Environ.*, 206, 174-188, <https://doi:10.1016/j.rse.2017.12.024>, 2018.

781 Liu, Y., Yang X., Wang, E., and Xue, C.: Climate and crop yields impacted by ENSO episodes on the
782 North China Plain: 1956-2006, *Reg. Environ. Change.*, 14(1), 49-59, [https://doi:10.1007/s10113-013-](https://doi:10.1007/s10113-013-0455-1)
783 0455-1, 2014.

784 Mercado, L., Bellouin, N., Sitch, S., Boucher, O., Huntingford, C., Wild, M., Cox, P.: Impact of changes
785 in diffuse radiation on the global land carbon sink, *Nature*, 458(7241), 1014-1017,
786 <https://doi:10.1038/nature07949>, 2009.

787 Muñoz, S. J.: ERA5-Land monthly averaged data from 1950 to present. Copernicus Climate Change
788 Service (C3S) Climate Data Store (CDS) [data set], 2019.

789 Norman, J. M.: Simulation of microclimates, in: *Biometeorology in Integrated Pest Management*, edited
790 by: Hatfield, J., Thomason, I., 65–99, New York, CA: Academic Press, 1982.

791 Piao, S., Sitch, S., Ciais, P., Friedlingstein, P., Peylin, P., Wang, X., Ahlstrom, A., Anav, A., Canadell,
792 J., Cong, N., Huntingford, C., Jung, M., Levis, S., Levy, PE., Li, J., Lin, X., Lomas, M., Lu, M., Luo,
793 Y., Ma, Y., Myneni, R., Poulter, B., Sun, Z., Wang, T., Viovy, N., Zaehle, S., and Zeng, N.: Evaluation
794 of terrestrial carbon cycle models for their response to climate variability and to CO₂ trends. *Global*
795 *Change Biol.*, 2117–2132, <https://doi.org/10.1111/gcb.12187>, 2013.

796 Piao, S., Wang, X., Wang, K., Li, X., Bastos, A., Canadell, J., Ciais, P., Friedlingstein, P., and Sitch, S.:
797 Interannual variation of terrestrial carbon cycle: Issues and perspectives, *Global Change Biol.*, 26(1),
798 300-318, <https://doi:10.1111/gcb.14884>, 2020.

799 Ryu, Y., Berry J., and Baldocchi, D.: What is global photosynthesis? History, uncertainties and
800 opportunities, *Remote Sens. Environ.*, 223, 95-114, <https://doi:10.1016/j.rse.2019.01.016>, 2019.

801 Saji, N., Goswami, B, Vinayachandran P, and Yamagata, T.: A dipole mode in the tropical Indian Ocean,
802 *Nature*, 401(6751), 360-363, <https://doi:10.1038/43855>, 1999.

803 Saji, N., and Yamagata, T.: Possible impacts of Indian Ocean Dipole mode events on global climate,
804 *Clim. Res.*, 25(2), 151-169, <https://doi:10.3354/cr025151>, 2003.

805 Sanders-DeMott, R., Ouimette, A., Lepine, L., Fogarty, S., Burakowski, E., Contosta, A., Ollinger, S.:
806 Divergent carbon cycle response of forest and grass-dominated northern temperate ecosystems to record
807 winter warming. *Global Change Biol.*, 26(3): 1519-1531, <https://doi.org/10.1111/gcb.14850>, 2020.

808 Schimel, D., Stephens, B., and Fisher, J.: Effect of increasing CO₂ on the terrestrial carbon cycle, P.

809 Natl. Acad. Sci. USA., 112(2), 436-441, <https://doi:10.1073/pnas.1407302112/-/DCSupplemental>,
810 2015.

811 Wang, J., Zeng, N., and Wang, M.: Interannual variability of the atmospheric CO₂ growth rate: roles of
812 precipitation and temperature, *Biogeo.*, 13(8), 2339-2352, <https://doi:10.5194/bg-13-2339-2016>, 2016.

813 Wang, J., Zeng, N., Wang, M., Jiang, F., Chen, J., Friedlingstein, P., Jain, A., Jiang, Z., Ju, W., Lienert,
814 S., Nabel, J., Sitch, S., Viovy, N., Wang, H., and Wiltshire, A.: Contrasting interannual atmospheric CO₂
815 variabilities and their terrestrial mechanisms for two types of El Niños, *Atmos. Chem. Phys.*, 18(14),
816 10333-10345, <https://doi:10.5194/acp-18-10333-2018>, 2018.

817 Wang, J., Liu, Z., Zeng, N., Jiang, F., Wang, H., and Ju, W.: Spaceborne detection of XCO₂ enhancement
818 induced by Australian mega-bushfires, *Environ. Res. Lett.*, 15(12), [https://doi:10.1088/1748-](https://doi:10.1088/1748-9326/abc846)
819 9326/abc846, 2020.

820 Wang, J., Jiang, F., Wang, H., Qiu, B., Wu, M., He, W., Ju, W., Zhang, Y., Chen, J., and Zhou, Y.:
821 Constraining global terrestrial gross primary productivity in a global carbon assimilation system with
822 OCO-2 chlorophyll fluorescence data, *Agr. Forest Meteorol.*, 304-305,
823 <https://doi:10.1016/j.agrformet.2021.108424>, 2021a.

824 Wang, J., et al.: Modulation of Land Photosynthesis by the Indian Ocean Dipole: Satellite-Based
825 Observations and CMIP6 Future Projections, *Earth's Future*, 9(4), <https://doi:10.1029/2020ef001942>.
826 2021b.

827 Wang, M., Wang, J., Cai, Q., Zeng, N., Lu, X., Yang, R., Jiang, F., Wang, H., and Ju, W.: Considerable
828 Uncertainties in Simulating Land Carbon Sinks Induced by Different Precipitation Products, *J. Geophys.*
829 *Res. - Biogeo.*, 126(10), e2021JG006524, <https://doi.org/10.1029/2021JG006524>. 2021c.

830 Wang, J., Jiang, F., Ju, W., Wang, M., Sitch, S., Arora, V., Chen, J., Goll, D., He, W., Jain, A., Li, X.,
831 Joiner, J., Poulter, B., Seferian, R., Wang, H., Wu, M., Xiao, J., Yuan, W., Yue, X., Zaehle, S.: Enhanced
832 India-Africa Carbon Uptake and Asia-Pacific Carbon Release Associated With the 2019 Extreme
833 Positive Indian Ocean Dipole, *Geophys. Res. Lett.*, 49(22), <https://doi:10.1029/2022gl100950>, 2022.

834 Wang, J., et al.: Anomalous Net Biome Exchange Over Amazonian Rainforests Induced by the 2015/16
835 El Niño: Soil Dryness-Shaped Spatial Pattern but Temperature-dominated Total Flux, *Geophys. Res.*
836 *Lett.*, 50(11), <https://doi:10.1029/2023GL103379>, 2023.

837 Williams, C., and Hanan, N.: ENSO and IOD teleconnections for African ecosystems: evidence of
838 destructive interference between climate oscillations, *Biogeo.*, 8(1), 27-40, [https://doi:10.5194/bg-8-](https://doi:10.5194/bg-8-27-2011)
839 27-2011, 2011.

840 Yan, R., Wang, J., Ju, W., Goll, D., Jain, A., Sitch, S., Tian, H., Benjamin, P., Jiang, F., and Wang, H.:
841 Interactive effects of the El Niño-Southern Oscillation and Indian Ocean Dipole on the tropical net
842 ecosystem productivity, *Agr. Forest Meteorol.*, 336, 109472,
843 <https://doi.org/10.1016/j.agrformet.2023.109472>, 2023.

844 Yang, R., Wang, J., Zeng, N., Sitch, S., Tang, W., McGrath, M., Cai, Q., Liu, D., Lombardozzi, D., Tian,
845 H., Jain, A., and Han, P.: Divergent historical GPP trends among state-of-the-art multi-model
846 simulations and satellite-based products, *Earth Syst. Dynam.*, 13(2), 833-849, [https://doi:10.5194/esd-](https://doi:10.5194/esd-13-833-2022)
847 13-833-2022, 2022.

848 Yang, Y., S.-P. Xie, L. Wu, Y. Kosaka, N.-C. Lau, and G. A. Vecchi.: Seasonality and Predictability of
849 the Indian Ocean Dipole Mode: ENSO Forcing and Internal Variability, *J. Climate*, 28(20), 8021-8036,
850 <https://doi:10.1175/JCLI-D-15-0078.1>, 2015.

851 Ying, K., Peng, J., Dan, L., and Zheng, X.: Ocean—atmosphere Teleconnections Play a Key Role in the
852 Interannual Variability of Seasonal Gross Primary Production in China, *Adv. Atmos. Sci.*, 39(8), 1329-
853 1342, <https://doi:10.1007/s00376-021-1226-4>, 2022.

854 Zeng, N., Mariotti, A., and Wetzel, P.: Terrestrial mechanisms of interannual CO₂ variability, *Global*
855 *Biogeochem Cy.*, 19(1), <https://doi:10.1029/2004gb002273>, 2005.

856 Zhang, X., Wang, Y., Peng, S., Rayner, P., Ciais, P., Silver, J., Piao, S., Zhu, Z., Lu, X., Zheng, X.:
857 Dominant regions and drivers of the variability of the global land carbon sink across timescales, *Global*
858 *Change Biol.*, 24(9), 3954-3968, <https://doi:10.1111/gcb.14275>, 2018.

859 Zhang, Y., Dannenberg, M., Hwang, T., and Song, C.: El Niño-Southern Oscillation-Induced Variability
860 of Terrestrial Gross Primary Production During the Satellite Era, *J. Geophys. Res. - Biogeo.*, 124(8),
861 2419-2431, <https://doi:10.1029/2019jg005117>, 2019.

862 Zhang, Y., Zhou, W., Wang, X., Wang, X., Zhang, R., Li, Y., and Gan, J.: IOD, ENSO, and seasonal
863 precipitation variation over Eastern China, *Atmos. Res.*, 270,
864 <https://doi:10.1016/j.atmosres.2022.106042>, 2022a.

865 Zhang, Y., Zhou, W., Wang, X., Chen, S., Chen, J., and Li, S.: Indian Ocean Dipole and ENSO's
866 mechanistic importance in modulating the ensuing-summer precipitation over Eastern China, *NPJ Clim.*
867 *Atmos. Sci.*, 5(1), <https://doi:10.1038/s41612-022-00271-5>, 2022b.

868 Zhu, Z., Piao, S., Xu, Y., Bastos, A., Ciais, P., and Peng, S.: The effects of teleconnections on carbon
869 fluxes of global terrestrial ecosystems, *Geophys. Res. Lett.*, 44(7), 3209-3218,
870 <https://doi:10.1002/2016GL071743>, 2017.